Compensation walls in gallium and aluminum substituted gadolinium–bismuth–iron garnet films created by laser annealing: Measurements and simulations

L. Wilkens, D. Träger, and H. Dötsch[a)]
University of Osnabrück, 49069 Osnabrück, Germany

A. M. Alexeev and A. F. Popkov
State Research Institute of Physical Problems, NT-MDT, 103460 Moscow, Russia

V. I. Korneev
Moscow Institute of Electronic Technology, 103482 Moscow, Russia

Magnetic garnet films of composition $(Gd_2 Bi_1) (Fe_{4.3} Ga_{0.2} Al_{0.5}) O_{12}$ are grown by liquid phase epitaxy on (111) oriented substrates of gadolininium–gallium–garnet close to magnetic compensation. Local compensation walls (CW) are fabricated by laser annealing. Images of parallel and antiparallel compensation walls and of Bloch walls in annealed regions are obtained by magnetic force microscopy (MFM). The MFM signals associated with the CWs turned out to be smaller in amplitude but broader in space than the signals created by Bloch walls. To simulate the experimental results a theoretical model is developed taking into account the broadening of the CW by the preparation technique. Very good agreement between measurements and numerical simulations is obtained. © *2003 American Institute of Physics.* [DOI: 10.1063/1.1544646]

I. INTRODUCTION

Compensation walls (CW) are a special kind of 180° magnetic walls. They were discovered about 30 years ago in gallium substituted yttrium–iron–garnet (YIG) films having a lateral gradient of the gallium content.[1,2] The origin of such walls is connected with the gallium distribution between the iron sublattices. The basic sublattice magnetizations at compensation walls is sketched in Fig. 1 and compared to those of a Bloch wall (BW). The saturation magnetization M_s is the net magnetization given by the vectorial sum of dodecahedral $\mathbf{M}_c$, octahedral $\mathbf{M}_a$ and tetrahedral $\mathbf{M}_d$ sublattice magnetizations. In the case of a Bloch wall all sublattice magnetizations conserve their magnitudes but change their direction at the domain boundary, see Fig. 1(c).

At a compensation wall the sublattice magnetizations $|\mathbf{M}_a|$ and $|\mathbf{M}_d|$ of the octahedral and tetrahedral sublatice change their magnitude such that on one side of the wall $|\mathbf{M}_d|$ is larger than $|\mathbf{M}_a| + |\mathbf{M}_c|$ and vice versa on the other side. In the case of an antiparallel compensation wall, Fig. 1(a), the sublattice magnetizations have the same directions on both sides of the wall but the net magnetizations are oppositely oriented. In the case of a parallel compensation wall, Fig. 1(b), the sublattice magnetizations have opposite directions on both sides of the wall while the net magnetizations are parallel. The antiparallel compensation wall can easily be transformed into a parallel one by applying a bias field perpendicular to the film plane. In the following, the left hand side of Figs. 1(a) and 1(b) corresponds to the annealed region, the right hand side to the unannealed region.

The equilibrium distribution of gallium/aluminum and iron between octahedral and tetrahedral sites depends on the temperature. At low temperatures the tetrahedral sites are higher populated by gallium/aluminum than the octahedral sites.[3–5] Therefore, the ion distribution between these lattice sites and thus the sublattice magnetizations can be controlled by annealing at different temperatures. If annealing is carried out at high temperatures, the state of equilibrium is reached rapidly. By quenching the sample to room temperature the high temperature equilibrium state is frozen in.

Directly at a CW the net magnetization is zero. As the sublattice magnetizations depend on temperature the location of a CW is characterized by a compensation temperature T_c with $M_s(T_c) = 0$. All compensation walls considered in this article are based on a local redistribution of gallium/aluminum and iron between octahedral and tetrahedral lattice sites induced by laser annealing. The total gallium/aluminum and iron contents are constant across the CW. Thus, the total spin quantum number per unit cell is the same on both sides of the compensation wall. However, the magnitudes of the net magnetizations need not be equal on both sides of a CW.

Figure 1 shows the sublattice magnetizations outside the magnetic walls. The variations of the sublattice magnetizations across compensation walls are sketched in Fig. 2. In principle, the redistribution of gallium/aluminum and iron can take place within two neighboring unit cells. However, due to the preparation of the CW by laser annealing the redistribution takes place gradually over many unit cells and extends over a distance in the range of some micrometers, see below. On the other hand, the change of direction of the sublattice magnetizations of a parallel CW (see Figs. 1 and 2) is determined by the ratio between the exchange constant A and the uniaxial anisotropy constant K_u. This is similar to
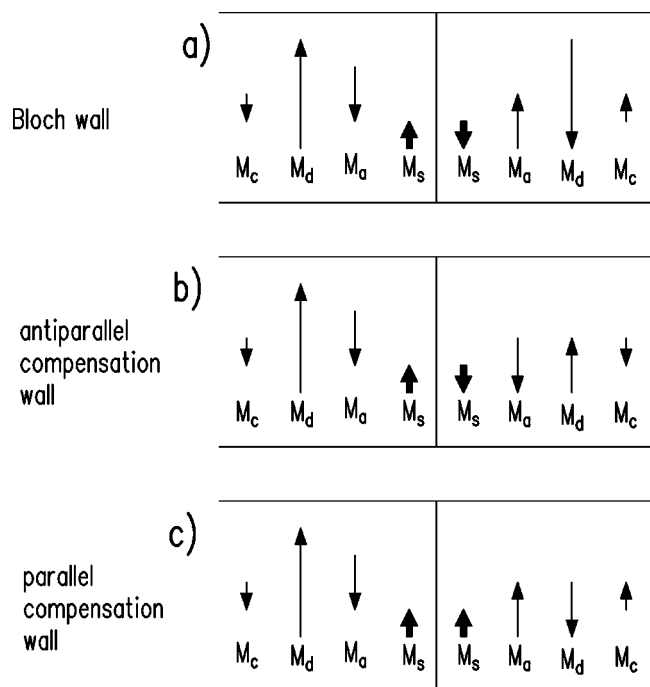
FIG. 1. Sublattice magnetizations on both sides of an antiparallel compensation wall (a), of a parallel compensation wall (b) and of a Bloch wall (c), for gallium/aluminum substituted iron garnet films near compensation. M_s denotes the net magnetization and M_i the sublattice magnetizations where the index i refers to the octahedral, tetrahedral and dodecahedral sublattices, respectively.

the case of a BW, having a wall width parameter $\Delta_0 = \sqrt{A/K_u}$. This width is about 0.1 μm.[6] Thus, the magnetic width of a parallel CW is about the same as that of a BW and therefore much smaller than the width of the transient region where the redistribution occurs. As the Faraday rotation depends on the direction of the sublattice magnetizations, the parallel CW shows a sharp and strong Faraday contrast, while for an antiparallel CW the contrast is weak.

Compensation wall domains have been proposed for magneto-optic storage applications.[2] Laser annealed (Bi, Ga):YIG films with a periodic pattern of compensation walls were used to realize integrated magneto-optic isolators based on nonreciprocal TE–TM mode conversion.[7] Ando, Okoshi, and Koshizuka applied laser annealing to modify locally the

magnetic properties of garnet films.[8] Recently compensation walls attracted attention for new concepts of integrated optical isolators based on nonreciprocal optical mode interference. By CWs a strong spatial gradient of the Faraday rotation in gyrotropic waveguides can be achieved, which induces a high nonreciprocal phase shift between forward and backward propagating optical modes. This is the basis of nonreciprocal Mach–Zehnder interferometers to realize integrated optical isolators.[9]

The nonreciprocal phase shift for TM modes is induced by CWs parallel to the film plane. Such walls are easily obtainable by double layers.[10] On the other hand, vertical CWs at the center of optical waveguides are needed for the nonreciprocal phase shift of TE modes. Although such a phase shift can also be induced by BWs,[11,12] CWs have the advantage of having a stable location in the presence of a magnetic field.[13,14]

It is very important to know the magnetic and spatial structure of the CW to control the magneto-optic properties of the nonreciprocal waveguides. To measure the spatial variation of the magnetization across a CW, magnetic force microscopy (MFM) is a very attractive tool. This technique has been applied successfully for imaging magnetic domains and domain walls in garnets and other magnetic materials.[15–17] However, compensation walls have not yet been investigated by MFM methods.

II. EXPERIMENTS

Ferrimagnetic garnet films of composition $(Gd_2 Bi_1)(Fe_{4.3} Ga_{0.2} Al_{0.5})O_{12}$ are grown by liquid phase epitaxy on (111) oriented substrates of gadolinium gallium garnet. At first the films are globally annealed in vacuum. Temperature and duration of this procedure are chosen such that the global compensation temperature of the film is shifted to about 350 K, well above room temperature. The sample used for the investigations has film thickness of 5.0 μm.

For laser annealing a frequency doubled Nd:yttrium–aluminium–garnet laser at 532 nm wavelength is used. The output power can be adjusted up to 190 mW. The laser is focused to a spot of about 6 μm radius. The laser is moved at a speed of 1.5 cm/s across the sample. Using scanning technique at a line period of 5 μm, annealed regions of 100 μm width and 6 mm length are generated. Several regions of this kind are produced being separated by unannealed strips of 100 μm width.

The annealing procedure shifts the compenstaion temperature below room temperature. Thus, the Faraday rotation has an opposite sign in the annealed and unannealed regions when the net magnetization of the film is saturated perpendicular to the film plane by an external magnetic field. This allows the visualization of the annealed patterns in the film as shown in Fig. 3(a). However, if unpolarized light is used, Fig. 3(b), a few patterns are still visible due to scattering. In this case the film is damaged because the laser power was too high during annealing.

Magneto-optic observations show that the annealed regions can easily be demagnetized by the generation of stripe
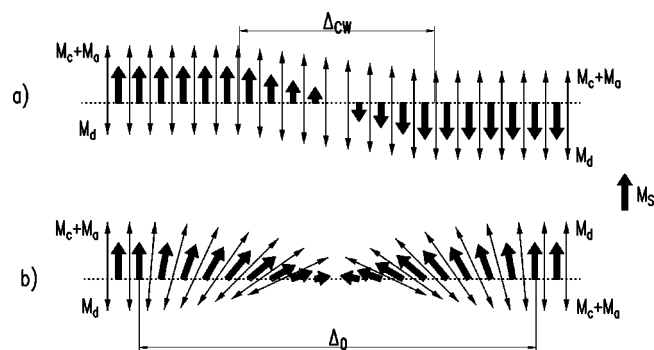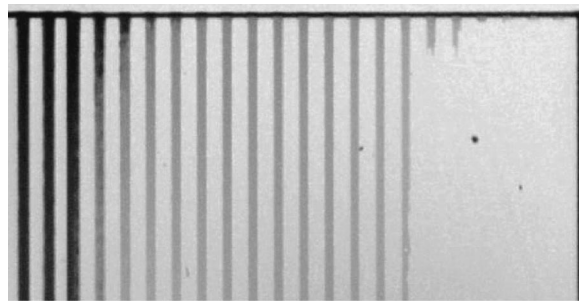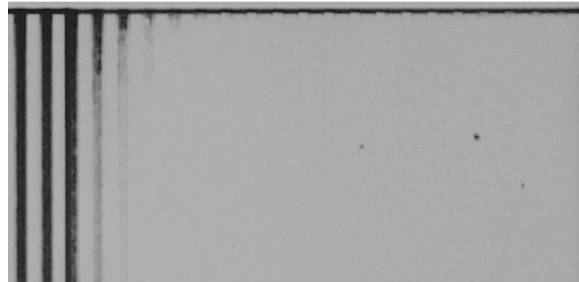

FIG. 2. Variation of the sublattice magnetizations and of the net magnetization across an antiparallel compensation wall (a) and a parallel one (b). This figure is not to scale, the width Δ_{CW} of the CW is much larger than Δ_0.

(a)

(b)

FIG. 3. Optical transmission image of patterns fabricated by scanning laser beam annealing in a gallium/aluminum substituted iron garnet film near compensation. (a) Polarized light (Faraday rotation), (b) unpolarized light (scattering). The dark strips of width 100 μm are the annealed regions.

domains using an external field. This means that the magnetization of the annealed regions is higher than that of the unannealed regions, which are closer to compensation.

Using magnetic force microscopy, the variation of the magnetization across a CW can be derived. For this purpose the scanning probe microscope SOLVER 47H (NT–MDT, Russia) and the two pass technique with ac or resonant mode MFM measurement is used. The magnetic probe is a silicon cantilever tip covered by 50 nm cobalt. The cone shaped cantilever tip has a typical height of 2–8 μm and the cone angle is 20–30°, see Fig. 4.

At first the surface topography is measured in the contact mode using a very low flying height. In this mode van der Waals tip–sample interaction prevails. In the second step the cantilever moves at larger constant tip–sample distance for
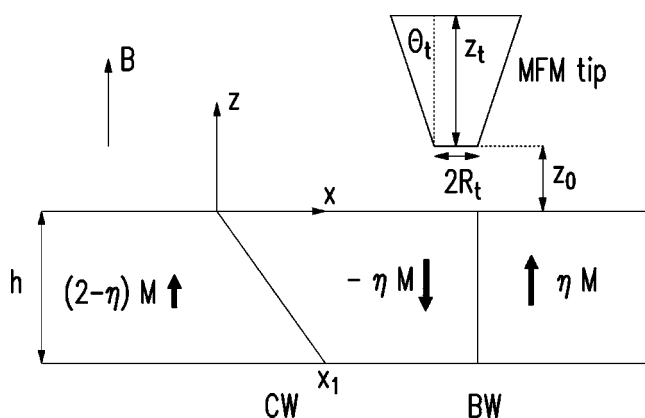

FIG. 4. Sketch of the considered MFM tip and the ferrimagnetic garnet film with Bloch wall and antiparallel CW.
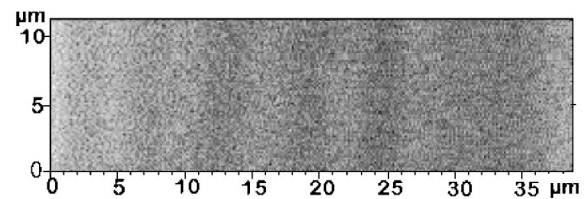

FIG. 5. MFM image of an annealed region showing tracks of the scanning laser annealing procedure.

typical flying heights of $z_0 = 50$ nm. The magnetic signal is measured as the oscillating cantilever phase shift caused by the long-distance magnetic tip–sample interaction. Magnetization states of the magnetic garnet film are also determined by magneto-optic observations.

Topographic atomic force measurements in the contact mode confirm that the film surface in the annealed regions is not changed significantly if the laser power does not exceed the threshold value for damaging. Magnetic imaging of annealed patterns in saturated films shows slightly visible parallel magnetic traces associated with the laser beam tracks as demonstrated in Fig. 5. The periodicity corresponds to the scanning period. This effect means that the laser annealing creates slightly nonuniform spatial redistributions of gallium/aluminum ions across the laser track.

After the demagnetization of the film and generation of stripe domains in the annealed pattern, two different kinds of MFM signals are observed during MFM scanning perpendicular to the laser tracks. One signal of smaller amplitude is shown in Fig. 6. It occurs at the interface between the annealed (left) and unannealed (right) regions of the film and it has a broad spatial variation. It does not change its position by applying a magnetic field and it is associated with an antiparallel CW. The abovementioned weak periodic traces created by the laser beam in the annealed region are slightly visible on the left side of the CW.

The other signal, shown in Fig. 7, is associated with Bloch walls, which can clearly be checked by the magneto-optic method. This signal has higher MFM contrast and changes its space position simultaneously with the observed magneto-optic domain boundary at the action of an external magnetic field as also demonstrated in Fig. 7. The top of the figure is different from the bottom because the Bloch walls are shifted by applying an external magnetic field.

It turns out that the shift of the BWs takes place in discrete steps corresponding to the periodicity of the observed annealing tracks. This stepwise shift of a Bloch wall towards
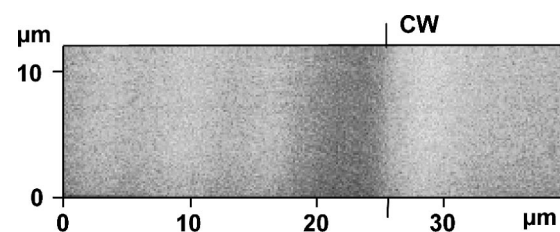

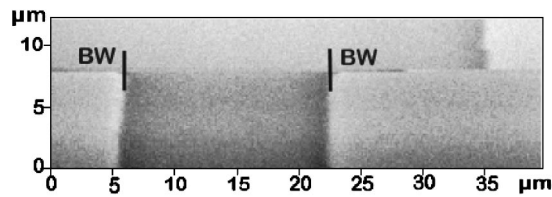FIG. 6. MFM image of an antiparallel compensation wall.

FIG. 7. MFM image of two Bloch walls formed in the annealed region. The top of the figure shows the changed magnetic structure in the same region after application of an external magnetic field during MFM scanning.

a CW at the action of an applied external field is illustrated in Fig. 8. Obviously there occurs some pinning of BWs by the annealing tracks.

It is seen that the MFM signal created by the Bloch wall has a higher amplitude than that of the CW. This result is connected to the broadening of the CW and to the increased net magnetization by laser annealing. Spatial broadening of the MFM signal created by antiparallel CWs is related to the diffusion origin of the CW formation as will be shown below by theoretical analysis.

When the external field is strong enough to annihilate the BW and the antiparallel CW, the magnetic film is saturated magnetically and the antiparallel CW is transformed into a CW with parallel net magnetization on both sides. The MFM signal created by a parallel CW has very small amplitude, see Fig. 9. Obviously the noise is much larger than in the case of antiparallel CW or BW, see Figs. 6–8.

III. THEORY

The geometry for the following calculations is sketched in Fig. 4. The ferrimagnetic garnet film of thickness h contains a slanted antiparallel CW and a vertical Bloch wall. The domain walls are considered parallel to the y axis and the magnetizations inside the domains are directed either parallel or antiparallel to the z axis. The finite width of the Bloch wall is about 0.1 μm and will be neglected. It is close to the resolution limit of the MFM measurements which is given by $2R_t$. For the parameter R_t the realistic value of 50 nm is used in the following.
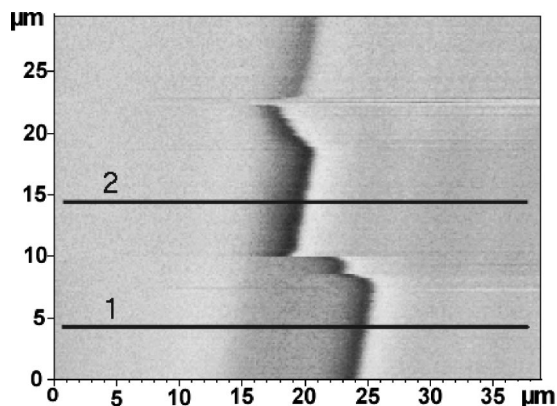

FIG. 8. MFM image of an antiparallel compensation wall and a Bloch wall. The latter is visible by higher contrast and can be shifted by an external magnetic field. The range of annealing lies in the right hand side of the figure.
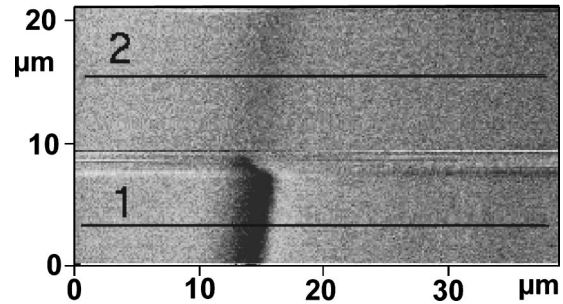

FIG. 9. MFM image of an antiparallel CW and a BW in the lower part of the figure. The parallel CW in the upper part is created by annihilation of the Bloch wall and the antiparallel CW using a saturating magnetic field.

The CW is assumed slanted by the distance x_1 across the film thickness. The reason for slanting is the temperature distribution during annealing as discussed in the Appendix. The saturation magnetization in the film is described by $M_{s,\text{an}} = \eta M$ in the annealed region and by $M_{s,\text{un}} = (2 - \eta)M$ in the unannealed part, where $M = (M_{s,\text{an}} + M_{s,\text{un}})/2$ is the mean magnetization value and the parameter $\eta = M_{s,\text{an}}/M$ characterizes the magnetization asymmetry on both sides of the CW. The periodicity observed in Fig. 5 is neglected and the film is assumed homogeneous on both sides of the wall. The magnetic probe is considered as a cone shaped tip with cone angle θ_t, cone height z_t, initial radius R_t and lift height z_0.

To simulate the MFM image of magnetic samples, it is necessary to calculate the shift of the cantilever oscillation frequency $\Delta\Omega_c$ caused by the tip–sample magnetostatic interaction.[15] The measured phase shift of oscillations is proportional to the shift of the resonance frequency, which is determined by the second derivative of the interaction energy $E_{tf}(z_0)$ with respect to the the distance z_0 between tip and film surface, i.e.

$$\Delta\Omega = (\Omega_c/2k_c)\cdot(\partial^2 E_{tf}/\partial z_0^2), \tag{1}$$

where Ω_c is the resonance frequency of the cantilever in absence of magnetic interactions and k_c is the cantilever stiffness. The magnetostatic dipole–dipole interaction can be calculated by the relation

$$E_{tf}(z_0) = \frac{\mu_0}{4\pi}\int\int\left(\frac{\mathbf{M}_t(\mathbf{r}_t)\cdot\mathbf{M}_f(\mathbf{r}_f)}{|\mathbf{r}_t - \mathbf{r}_f|^3}\right.$$
$$\left. - \frac{3[\mathbf{M}_t(\mathbf{r}_t)\cdot(\mathbf{r}_t - \mathbf{r}_f)][\mathbf{M}_f(\mathbf{r}_f)\cdot(\mathbf{r}_t - \mathbf{r}_f)]}{|\mathbf{r}_t - \mathbf{r}_f|^5}\right)d\mathbf{r}_t d\mathbf{r}_f. \tag{2}$$

The integration runs over the tip and film magnetization configurations $\mathbf{M}_t(\mathbf{r}_t)$ and $\mathbf{M}_f(\mathbf{r}_f)$, where $\mathbf{r}_t$ denotes the location on the tip and $\mathbf{r}_f$ the location on the garnet film, respectively.

First we consider a single perpendicular domain wall of zero width. The MFM magnetic tip is approximated by a magnetic dipole localized at the point $\mathbf{r}_0 = (x_t, 0, z_0)$, having dipole moment $\mathbf{M}_t(\mathbf{r}_t) = v\mathbf{M}_{0t}\delta(\mathbf{r}_0 - \mathbf{r}_t)$, where $\mathbf{M}_{0t} = (0, 0, M_t)$, v denotes the tip volume, and δ the Kronnecker

deltafunction. The integration in Eq. (2) over the two-dimensional magnetization configuration of the sample $M_f(\mathbf{r}_f)=[0,0,M_f(x_f,z_f)]$ leads to the following expression for the MFM signal $\Delta\Omega_{\mathrm{MFM}}(x,z_0)$:

$$\Delta\Omega_{\mathrm{MFM}}(x,z_0)=\frac{\Omega_c v \mu_0 M_t}{2\pi k_c}\int_{-\infty}^{+\infty}dx_f\frac{\partial}{\partial z_0}$$

$$\times\int_{-h}^{0}\left(\frac{4(z_0-z_f)^3}{[(z_0-z_f)^2+(x-x_f)^2]^3}\right.$$

$$\left.-\frac{3(z_0-z_f)}{((z_0-z_f)^2+(x-x_f)^2)^2}\right)M_f(x_f,z_f)dz_f.$$

$$(3)$$

The considered isolated perpendicular domain wall is assumed located at the point $x_f=0$ with a stepwise change of the magnetization $M_f(x_f)=M[\theta(x_f)-\theta(-x_f)]$, where θ denotes the Heavyside stepfunction. In this case the two-dimensional integral in Eq. (3) can be reduced by partial integration to simple integrals over magnetic charges on the top and bottom surfaces yielding the final result

$$\Delta\Omega_{\mathrm{MFM}}(x,z_0)=A\left(\frac{2(z_0+h)x}{[(z_0+h)^2+x^2]^2}-\frac{2z_0x}{(z_0^2+x^2)^2}\right),\quad(4)$$

where $A=\Omega_c v \mu_0 M_0 M_t/2\pi k_c$ is a normalizing factor. It is clear from this relation that for $z_0\ll h$ the MFM image will have two very sharp signal peaks near the domain wall separated by the distance $\Delta x\sim z_0$, see curve 1 in Fig. 10.

For example, if we put $h=2$ μm and $z_0=0.05$ μm, then we get sharp peaks at $x\sim\pm0.025$ μm. This behavior does not correspond to the experimental MFM measurements of the wall, where the MFM signal has long tails and peak separation in the range $\Delta x\sim4$ μm. The simulation leads to broader peaks with smaller signal amplitude, if larger tip distances of $z_0=0.5-1$ μm are used. However, such values of the tip lifting are not realistic.

To improve the agreement with the experimental results we have to improve the simple dipole model of the tip. For this purpose we introduce the cone model, where the MFM signal is averaged over the cone shaped magnetic cantilever tip shown in Fig. 4. For this model the MFM signal can be calculated by
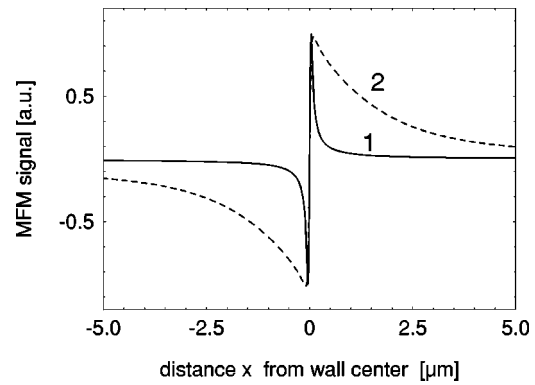

FIG. 10. Simulated MFM signal created by an isolated infinitely thin domain wall for the dipole model (1), Eq. (4), and cone tip model (2), Eq. (5). Calculation parameters are $h=2$ μm, $z_0=0.05$ μm, $\eta=1$.

$$\Delta\Omega_{\mathrm{MFM}}(x,z_0)=A_0\int_0^{z_t}dz\int_0^{2\pi}\Delta\Omega_{\mathrm{MFM}}(x+(R_t$$

$$+z\tan\theta_t)\cos\varphi,z+z_0)\cdot(R_t$$

$$+z\tan\theta_t)d\varphi.$$

$$(5)$$

A_0 is the signal normalizing factor. This factor is considered as one of the adjustment parameters of the calculated MFM signal. The tip parameters are cone angle $\theta_t=20°$, the initial radius $R_t=50$ nm and the height $z_t=3\mu$ m. Using this model, reasonable MFM signals are achieved for an isolated domain wall, at least in the region of the tails as shown in Fig. 10, curve 2.

According to the MFM measurements, the signal of the compensation wall is lower than that of the ordinary Bloch wall formed in the annealed region and seems to be significantly broader in characteristic peaks and tails. We consider two possible mechanisms of CW broadening. One originates from the CW diffusive broadening in the transitional region and another one from the slant of the CW through the film thickness.

Consider an antiparallel slanted CW as shown in Fig. 4, which has magnetization transition from the value $M_f=(2-\eta)M$ in the unannealed region to $M_f=\eta M$ in the annealed part. For the spatial variation of the magnetization of such an antiparallel CW the following approximation is assumed:

$$M_f(x,z)=\begin{cases}(2-\eta)M & (x-x_m)<-\Delta_{\mathrm{CW}},\\(1-\eta-(x-x_m)/\Delta_{\mathrm{CW}}-(1/\pi)\sin(\pi(x-x_m)/\Delta_{\mathrm{CW}})M & -\Delta_{\mathrm{CW}}<(x-x_m)<\Delta_{\mathrm{CW}},\\-\eta M & (x-x_m)>\Delta_{\mathrm{CW}},\end{cases}\qquad(6)$$

where the parameter Δ_{CW} takes into account the diffusive broadening of the CW and $x_m(z)$ with $0\leq x_m\leq x_1$ the slanting. In the following a linear slanting is assumed with $x_m(z)=x_1*|z|/h$. The variation given by Eq. (6) is depicted in Fig. 11, where the variation for a parallel CW is also shown. It is given by the absolute value of the magnetization of the antiparallel case.

The simulated MFM signal for such an antiparallel CW is shown by curve 1 in Fig. 12. It illustrates the influence of the slant which causes an asymmetric broadening of the MFM signal. There is only one sharp peak due to the stepwise change of magnetic charges of the CW at the upper film surface. The other peak is smoothed out due to the influence of bulk magnetic charges at the slanted CW. However, a
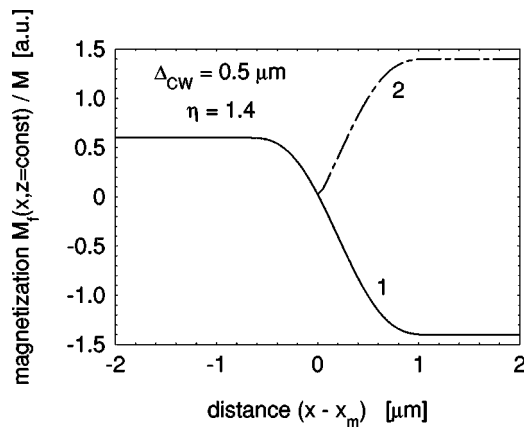
FIG. 11. Variation of the net magnetization through an antiparallel (curve 1) and a parallel compensation wall (curve 2) according to Eq. (6). x_1 = 3 μm, Δ_{CW} = 0.5 μm.

sharp peak is not observed experimentally. Curves 2 and 3 of Fig. 12 show the calculated effect of further broadening of the MFM signal peaks by increasing the CW width Δ_{CW}. The MFM signal of the antiparallel CW does not depend on the asymmetry factor η. This behavior is in contrast to that of a parallel CW, the MFM signal of which strongly depends on the CW asymmetry factor η.

To fit the experimental MFM data, the values of the normalizing factor A_0, CW half-width Δ_{CW}, slope extension distance x_1 and asymmetry parameter η are varied. For the other parameters the following fixed values are chosen: tip lifting z_0 = 0.1 μm, tip cone height z_t = 3 μm, cone angle θ_t = 20° and initial tip radius R_t = 50 nm. A comparison of the calculated MFM signals with measured MFM data for the antiparallel CW and a Bloch wall is presented in Fig. 13. Calculations and measurements are taken along the lines 1 and 2 of Fig. 8, which illustrate the shift of the BW by applying an external magnetic field.

Furthermore, the effect of Bloch wall annihilation and the simultaneous transformation of an antiparallel CW into a parallel one by applying a saturating magnetic field, which is shown in Fig. 9, is also simulated. Measured and calculated MFM signals along lines 1 and 2 of Fig. 9 are presented in Fig. 14. Calculations are made for η = 1.4, Δ_{CW} = 0.5 μm,

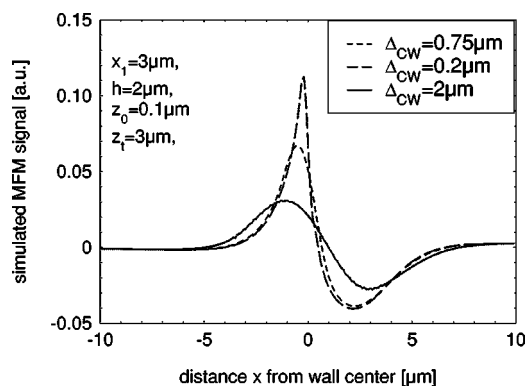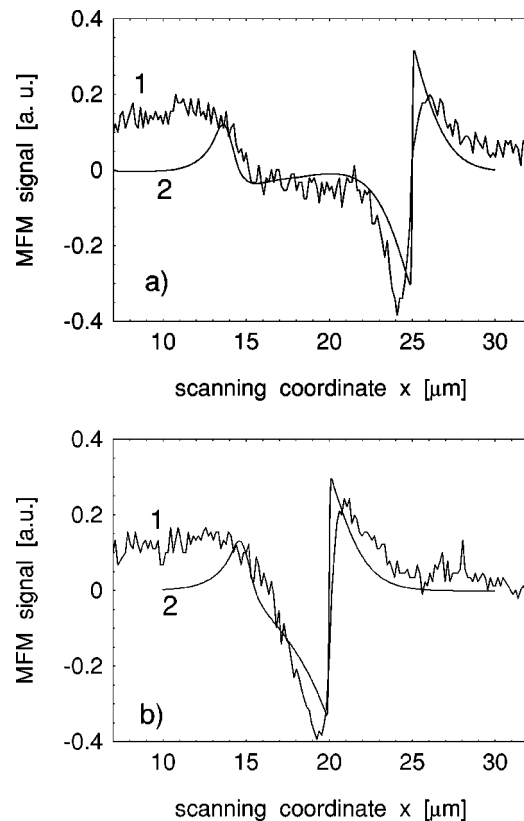FIG. 13. Measured (1) and simulated (2) MFM signals created by an antiparallel CW and a BW during scanning. (a) At line 1 and (b) at line 2 of Fig. 8. Calculations are made for η = 1.4, Δ_{CW} = 0.5 μm, z_0 = 0.1 μm, x_1 = 3 μm.

x_1 = 3 μm. A good agreement between the experimental data and the developed cone model is observed.

Vertical CWs at the center of optical rib waveguides have been used to induce a nonreciprocal phase shift of TE modes, aiming at the realization of integrated optical isolators.[13] It turned out that the measured phase shift was smaller than the calculated one. Probably, this discrepancy is caused by the slanting of the CW through the film thickness observed by the investigations presented in this article. A possible reduction of the slanting effect is discussed in the Appendix.

IV. CONCLUSIONS

The samples studied in this article are close to compensation at room temperature. In the laser annealed regions the net magnetization is higher so that magnetic domains nucleate. It is observed that the domain walls are pinned at magnetic traces caused by the annealing procedure. These traces have the same periodicity as the laser scanning.

The MFM signals of BWs are stronger than those of the antiparallel CWs due to the higher net magnetization in annealed regions. The BWs are shifted by external magnetic fields at discrete steps corresponding to the laser track periodicity. Parallel CWs show only low MFM signals due to the small change of magnetization between both sides of the CW.

FIG. 12. Simulated MFM signal of slanted antiparallel CW for different widths. Calculation parameters are h = 2 μm, z_0 = 0.1 μm, η = 1.
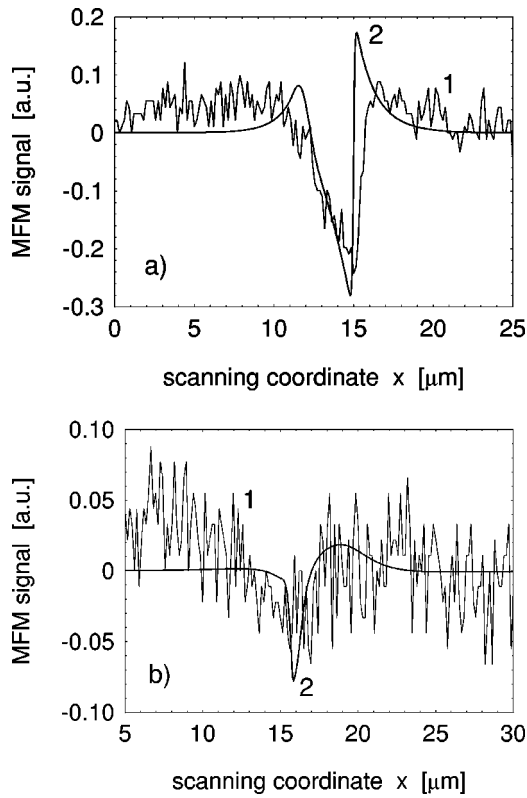
FIG. 14. Measured (1) and simulated (2) MFM signals created by a CW and a BW during scanning (a) at line 1 and (b) at line 2 of Fig. 9. Calculations are made for $\eta = 1.4$, $\Delta_{CW} = 0.5$ μm, $z_0 = 0.1$ μm, $x_1 = 3$ μm.

The theoretical analysis of the MFM signals obtained from CWs shows that, despite the adjustment of some parameters, it is necessary to take into account not only the diffusive mechanism of CW broadening, but also a slanting of the CW. This effect becomes plausible by the numerical calculation of the temperature distribution.

The results achieved in this article are important for the development of optical isolators using vertical CW.[13] The slant of the CW decreases the nonreciprocal effect and therefore must be kept as small as possible.

ACKNOWLEDGMENT

APPENDIX

The redistribution of Ga/Al and Fe between octahedral and tetrahedral lattice sites is temperature dependent as discussed by Röschmann.[3] Thus, the temperature distribution obtained in the garnet film by the absorbed laser beam is essential for the formation of CWs. The laser moves with the steady velocity $v_0 = 15$ mm/s along a straight line at the film surface. The laser heating creates a steady solitary wave of temperature distribution in the film. This steady state temperature variation will be calculated in the following.
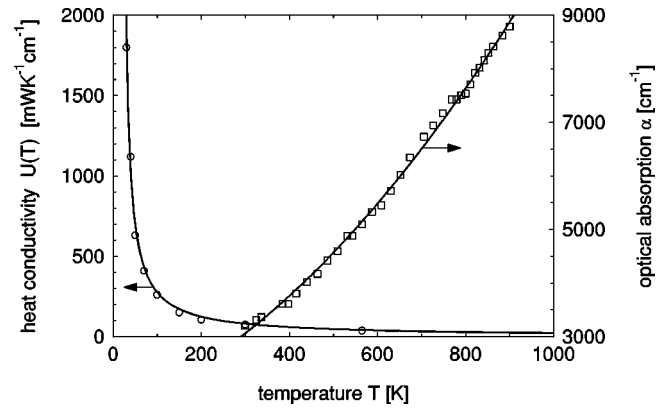

FIG. 15. Measured heat conductivity of YIG (see Ref. 18) and measured optical absorption for a film of $Gd_2Bi_1Fe_{4.3}Ga_{0.7}$ at $\lambda = 532$ nm vs temperature. The solid curves are fitted to the measurements, see Eqs. (A4) and (A5).

A half infinite solid space $z < 0$ is considered. It is illuminated by a laser beam of total power P_0 with Gaussian power distribution

$$P(r) = \frac{P_0}{2\pi R_0^2} \exp\left(-\frac{r^2}{2R_0^2}\right), \tag{A1}$$

where R_0 is the beam spot radius. The basic equation for calculating the temperature distribution induced by the absorbed laser power is the thermal diffusion equation

$$\nabla(U(T)\nabla T) = -F(T,r,z), \tag{A2}$$

where U is the heat conductivity and F denotes the thermal source which is given in cylindrical coordinates by

$$F(T,r,z) = \alpha(T)(1-R_r)P(r)\exp(-\alpha(T)|z|). \tag{A3}$$

$R_r = [(1-n)/(1+n)]^2$ is the reflection coefficient and α is the absorbtion coefficient. For the refractive index a constant value of $n = 2.2$ is used. The measured temperature dependencies of the heat conductivity and of the absorption coefficient are taken into account. These data are shown in Fig. 15. The optical absorption is determined at a wavelength of 532 nm for the sample $Gd_2Bi_1Fe_{4.3}Ga_{0.2}Al_{0.5}O_{12}$ used in this article. The heat conductivity of YIG is measured by Slack and Oliver.[18] It will be used for the investigated garnet film as well as for the substrate.

These experimental data can well be approximated by

$$U(T) = \frac{k}{T - T_k} \tag{A4}$$

with $k = 2.28$ mW/μm and $T_k = 17.5$ K and by

$$\alpha(T) = \frac{0.0054}{\text{cm K}^2}T^2 + \frac{3.21}{\text{cm K}}T + \frac{1614}{\text{cm}}. \tag{A5}$$

The boundary conditions are

$$\partial T/\partial z = 0$$

at the surface ($z = 0$, $0 \leq r < \infty$) and

$$T \to T_0, \quad \text{for} \quad R = \sqrt{r^2 + z^2} \to \infty,$$
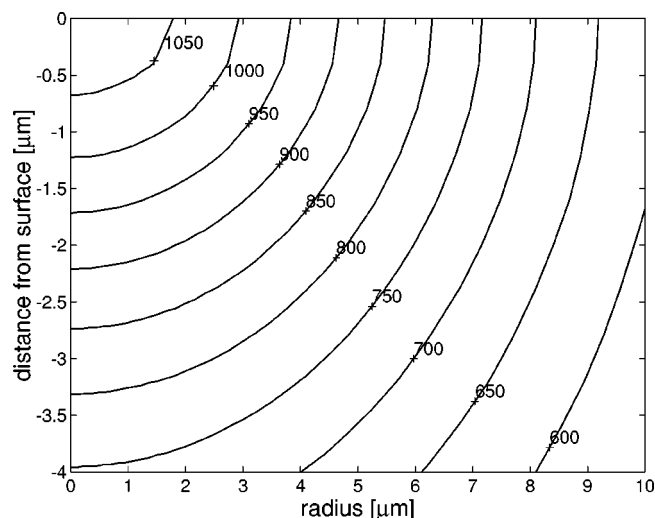
where $T_0 = 300$ K.

FIG. 16. Contour plot of the calculated temperature distribution for laser power of 120 mW and beam radius of 6 μm. The temperature dependence of the heat conductivity and of the optical absorption is taken into account.

FIG. 17. Contour plot of the calculated temperature distribution for laser power of 120 mW and beam radius of 6 μm for annealing through the substrate, which extends from $z = -4$ μm to $-\infty$. The temperature dependence of the heat conductivity and of the optical absorption is taken into account.

The left hand side of Eq. (A2) is reduced to the Laplace form by introducing a new variable

$$Y(r,z) = \ln\left(\frac{T(r,z) - T_k}{T_0 - T_k}\right). \tag{A6}$$

The characteristic velocity v_c of the heat flux as defined by Yong-Feng Lu[19] is

$$v_c = 2\sqrt{2}\,\frac{D(T)}{R_0} = 2\sqrt{2}\,\frac{U(T)}{R_0 C(T)}, \tag{A7}$$

where $D(T)$ is the heat diffusion coefficient and $C(T)$ the heat capacity. Using the data of $C(T)$ given by Shchelkotnov *et al.* for YIG,[20] it turns out that v_c varies between 1200 and 400 mm/s in the temperature range between 300 and 900 K. Thus, the scanning velocity of the laser beam of 15 mm/s is small compared to v_c and can be neglected.

Stationary solutions are looked for in infinite space $-\infty < z < +\infty$ symmetric with respect to the plane $z = 0$ to fulfill the first boundary condition $\partial T / \partial z = 0$. The diffusion equation is transformed by Green's function in cylindrical coordinates to the double integral over nonlinear thermal sources and solved by numerical integration and iteration procedure. Simulations were checked by some analytical solutions. Effects of thermal radiation are neglected.

The results of the calculation are shown as a contour plot in Fig. 16 for a total beam power of 120 mW and a beam radius of 6 μm. It is obvious that the lines of constant temperature are inclined with respect to the film normal. The temperature dependent redistribution of Ga/Al and Fe between octahedral and tetrahedral lattice sites thus induces a slanted compensation wall in the range of a few micrometers.

A considerable reduction of the slanting effect can be achieved if the laser enters the film through the substrate which is highly transparent at the laser wavelength. The simulated temperature distribution of this geometry is shown in Fig. 17. The substrate is assumed half infinite for $z < 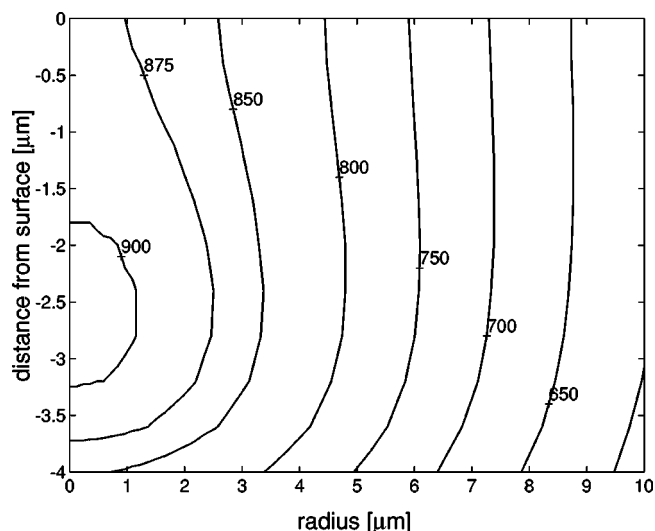-h$, see Fig. 4. It is essential to take into account the reflection of the laser light at the free surface of the film at $z = 0$. The reflection at the substrate-film interface is neglected because of the small difference of refractive indices. For this geometry the thermal source given by Eq. (A3) is replaced by

$$F(T,r,z) = \alpha(T)\,P(r)\,[\exp(+\alpha(T)|z|) + R_r$$
$$\times \exp(-\alpha(T)|z|)]\exp(-\alpha(T)h). \tag{A8}$$

The maximum temperature now occurs inside the film. This behavior is caused by the heat flow into the substrate. It is obvious that the new temperature distribution will cause much less slanting of the compensation wall. However, this effect has not yet been demonstrated experimentally.

[1] J.-P. Krumme and P. Hansen, Appl. Phys. Lett. **22**, 312 (1973).
[2] J.-P. Krumme and P. Hansen, Appl. Phys. Lett. **23**, 576 (1973).
[3] P. Röschmann, J. Phys. Chem. Solids **42**, 337 (1981).
[4] C. Borghese, J. Phys. Chem. Solids **28**, 2225 (1967).
[5] P. Hansen, H. Heitmann, and K. Witter, Phys. Rev. B **23**, 6085 (1981).
[6] A. P. Malozemoff and J. C. Slonczewski, *Magnetic Domain Walls in Bubble Materials* (Academic, New York, 1979).
[7] R. Wolfe, J. Hegarty, J. F. Dillon, Jr., L. C. Luther, K. G. Celler, L. E. Trimble, and C. S. Dorsey, IEEE Trans. Magn. **MAG-21**, 1647 (1985).
[8] K. Ando, T. Okoshi, and N. Koshizuka, IEEE Trans. Magn. **MAG-23**, 3485 (1987).
[9] J. Fujita, M. Levy, R. M. Osgood, Jr., L. Wilkens, and H. Dötsch, Appl. Phys. Lett. **76**, 2158 (2000).
[10] M. Wallenhorst, M. Niemöller, H. Dötsch, P. Hertel, R. Gerhardt, and B. Gather, J. Appl. Phys. **77**, 2902 (1995).
[11] A. F. Popkov, M. Fehndrich, M. Lohmeyer, and H. Dötsch, Appl. Phys. Lett. **72**, 2508 (1998).
[12] M. Fehndrich, A. Josef, L. Wilkens, J. Kleine-Börger, N. Bahlmann, M. Lohmeyer, P. Hertel, and H. Dötsch, Appl. Phys. Lett. **74**, 2918 (1999).
[13] L. Wilkens, D. Träger, A. F. Popkov, A. Alexeev, and H. Dötsch, Appl. Phys. Lett. **79**, 4292 (2001).
[14] O. Zhuromskyy, M. Lohmeyer, N. Bahlmann, H. Dötsch, P. Hertel, and A. F. Popkov, J. Lightwave Technol. **17**, 1200 (1999).
[15] D. Rugar, H. J. Mamin, and P. Guethner, S. E. Lambert, J. E. Stern, I. McFadyen, and T. Yogi, J. Appl. Phys. **68**, 1169 (1990).

[16] R. Proksch, K. Babcock, and J. Cleveland, Appl. Phys. Lett. **74**, 419 (1999).

[17] D. M. Donnet, J. N. Chapman, H. W. van Kersten, and W. B. Zeper, J. Magn. Magn. Mater. **115**, 342 (1992).

[18] G. A. Slack and D. W. Oliver, Phys. Rev. B **4**, 592 (1971).

[19] Y.-F. Lu, J. Appl. Phys. **71**, 3701 (1992).

[20] V. A. Shchelkotnov, V. N. Danilov, L. A. Reznitskii, and A. V. Korobeinikova, Inorg. Mat. (USSR, Engl. Transl.) **11**, 1396 (1975).